Evidence for Extraction of Photoexcited Hot Carriers from Graphene

Chang-Hua Liu, Nanditha M. Dissanayake, Seunghyun Lee, Kyunghoon Lee, and Zhaohui Zhong*

Department of Electrical Engineering and Computer Science, University of Michigan, Ann Arbor, Michigan 48109, United States

ABSTRACT

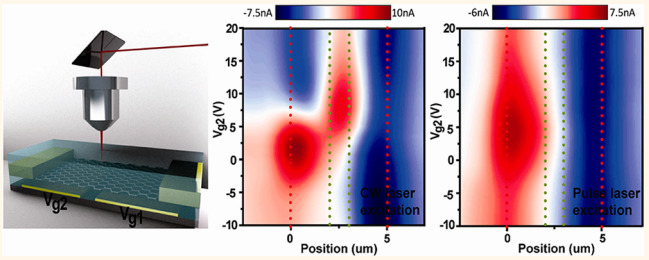

We report evidence of nonequilibrium hot carrier extraction from graphene by gate-dependent photocurrent study. Scanning photocurrent excited by femtosecond pulse laser shows unusual gate dependence compared with continuous wave (CW) laser excitation. Power dependence studies further confirm that the photocarriers extracted at the metal/graphene contact are nonequilibrium hot carriers. Hot carrier extraction is found to be most efficient near the Dirac point where carrier lifetime reaches a maximum. These observations not only provide evidence of hot carrier extraction from graphene but also open the door for graphene-based hot carrier optoelectronics.

KEYWORDS: graphene · hot carrier · scanning photocurrent imaging

Graphene, composed of single-layer carbon atoms, could be the potential material for hot carrier optoelectronic applications. The strong optical absorption of graphene (2.3% for a single atomic layer)[1,2] and the reduced phonon modes in low dimension indicate the possibility of creating nonequilibrium hot carriers due to inefficient cooling when the optical phonon temperature quickly rises to near hot carrier temperature under intense excitation.[3] In addition, as hot carriers cool below optical phonon energy (~200 meV), inefficient carrier−acoustic phonon relaxation process can further slow down carrier cooling.[4,5] Recently, hot carrier dynamics in graphene, including hot carrier diffusion,[6] carrier−carrier interaction,[7,8] carrier−phonon coupling and carrier recombination,[9−11] were investigated by femtosecond pulse laser. On the other hand, photocarrier transport in graphene, excited by a CW laser, was found to follow a built-in electric field[12−15] or photothermoelectric effect (PTE).[16−18] For the former mechanism, photoexcited electrons and holes are accelerated by a built-in electric field originating from the work function difference across the junction. In the latter mechanism, however, photothermoelectric current is driven by photocarrier diffusion when temperature gradient is established across the interface with different thermal power. Both mechanisms show photocurrent polarity reversal by tuning graphene doping concentration. Although it is still challenging to distinguish the dominant photocurrent generation mechanism,[17,19] recent studies at the graphene p−n junction suggest that inefficient electron−acoustic phonon relaxation will enhance the thermoelectric current, with a signature of multiple polarity reversals.[18,20,21]

To this end, we report photocurrent studies at the graphene−metal junction and graphene p−n junction by using both femtosecond pulse laser and CW laser excitation. Surprisingly, the gate-dependent photocurrent generated at the graphene−metal junction does not exhibit polarity reversal under pulse laser excitation. In addition, photocurrent peaks near the graphene Dirac point gate voltage, where photocarrier lifetime reaches a maximum based on theories.[22−24] The results provide the evidence of hot carrier generation and extraction from the graphene device. Also, the mechanism of photocurrent generation within the pristine graphene p−n junction is confirmed to be due to photothermoelectric effect.

RESULTS AND DISCUSSION

Figure 1a shows the schematic of a typical graphene p−n junction formed by electrostatic gating. A pair of split bottom gates (V_{g1} and V_{g2}) can electrostatically dope the graphene in the above sections into p- and n-type, respectively, and form the p−n junction in between (details in Supporting Information). Resistance *versus* split gate voltage scans exhibit consistent gate responses for

* Address correspondence to zzhong@umich.edu.

Received for review May 20, 2012 and accepted July 2, 2012.

Published online July 02, 2012
10.1021/nn302227r

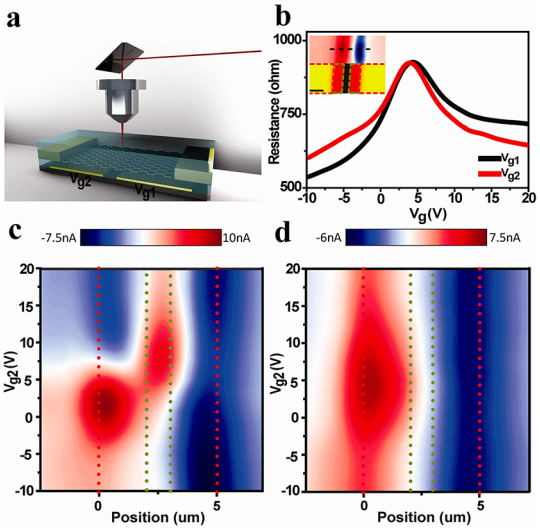

Figure 1. Striking difference for photocurrent generation in graphene between CW and pulse laser excitation. (a) Schematic drawing of the graphene device and experimental setup. (b) Gate response of the device with V_{sd} = 1 mV. The black curve shows resistance dependence on V_{g1} with V_{g2} grounded, and the red curve shows V_{g2} gate dependence with V_{g1} grounded. The top inset shows a spatially resolved two-dimensional photocurrent map with zero source−drain and gate bias voltage. The bottom inset shows optical reflection intensity map of the same graphene device. The red dashed lines indicate the boundary of the source and drain contacts, and the green dashed lines indicate the boundary of split bottom gates. Scale bar, 2 μm. (c) Gate-dependent photocurrent map under 3.8 mW CW laser excitation. (d) Gate-dependent photocurrent map under 3.8 mW pulse laser excitation. In both panels c and d, the red dotted lines indicate the source and drain contacts edges, and the green dotted lines indicate the bottom gates edges.

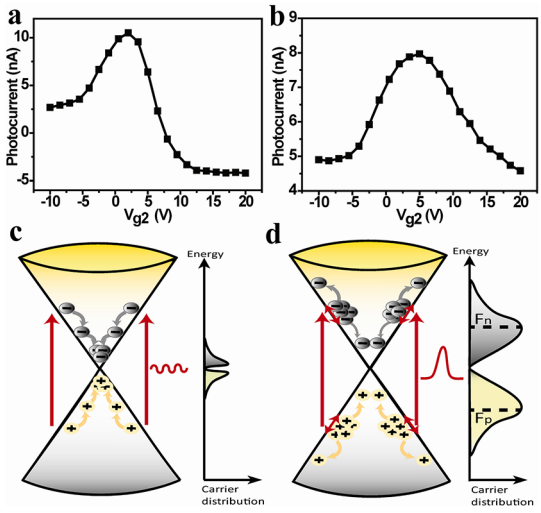

Figure 2. Extraction of photoexcited hot carriers from the graphene−metal junction. (a) Gate-dependent photocurrent at the metal contact edge under CW laser excitation. (b) Gate-dependent photocurrent at the metal contact edge under pulse laser excitation. (c) Schematic drawing of near-equilibrium carrier distribution under CW laser excitation. (d) Schematic drawing of nonequilibrium hot carrier distribution under pulse laser excitation.

both gates and a Dirac point gate voltage of ~4.8 V (Figure 1b). The device is studied by scanning photocurrent spectroscopy[13] (Figure 1a; also see Supporting Information) at ambient conditions. Briefly, we raster scan the excitation laser across the device and simultaneously measure the photocurrent and reflected light intensity. Both CW (λ = 900 nm) and femtosecond pulsed laser (λ = 800 nm) are used, and the focused laser spot sizes are around 1.5 μm. The top inset in Figure 1b shows a spatially resolved photocurrent map with CW excitation under zero source−drain and gate bias voltage. Photocurrent peaks at the source and drain metal−graphene contacts, confirmed by overlapping with the reflected light intensity mapping (Figure 1b, bottom inset).

We then turn our attention to the gate-dependent photocurrent mapping across the length of the device (dotted line in the top inset of Figure 1b) with both CW and pulse laser excitation. Figure 1c,d shows photocurrent *versus* V_{g2} and laser position for CW and femtosecond pulse excitation, respectively. V_{g2} is scanned from −10 to 20 V with V_{g1} grounded during the measurement, modulating the graphene device from p−p junction to p−n junction. Significantly, two distinct differences are observed by comparing the CW *versus* pulse laser excited photocurrent maps. First, photocurrent peaks at the p−n junction between the split gates with CW excitation (Figure 1c, position = 2.5 μm) but disappears when excited with pulse laser (Figure 1d, position = 2.5 μm). Second, photocurrent near the left metal/graphene junction also shows drastic difference for CW and pulse excitation. Under CW excitation, photocurrent switches sign at V_{g2} = 7.5 V (Figure 1c, position = 0). Surprisingly, with pulse excitation, photocurrent remains positive, and peaks at V_{g2} = 5 V (Figure 1d, position = 0). The same phenomena are also observed at the right metal/graphene contact when tuning V_{g1} gate voltages with V_{g2} grounded and reproducible among all devices tested.

We first focused our attention on the photocurrent abnormally at the metal/graphene contact between CW and pulse laser excitation. Figure 2a,b shows the gate-dependent photocurrent at the contact edge extracted from Figure 1c,d at position = 0, respectively. In Figure 2a, the photocurrent excited by the CW laser switches sign at V_{g2} = 7.5 V, agreeing with the literature where work function difference between graphene and metal determines the sign of photocurrent.[12,14,15] On the basis of the thickness of the gate dielectric (50 nm Al_2O_3, $\varepsilon \sim 7.5$) and the Dirac point voltage, we estimate a metal work function of 4.3 eV, consistent with the typical value for our contact metal Ti. In comparison, surprisingly, photocurrent excited by the pulse laser (Figure 2b) remains positive throughout the gate voltage sweep and peaks at V_{g2} = 5 V, which coincides with the Dirac point gate voltage.

Furthermore, the photocurrent curve exhibits nearly symmetrical decay around V_{g2} = 5 V by increasing either hole density or electron density.

The unusual photocurrent response from pulse laser excitation provides the evidence of nonequilibrium hot carrier extraction from graphene. Photogenerated hot carriers typically release energy to optical phonons within subpicosecond time scale, followed by slower relaxation through scattering with acoustic phonons and electron−hole recombination.[4,5] Hot carrier relaxation through carrier multiplication has also been reported in graphene recently.[18,25] Nevertheless, under CW excitation, photocarriers will relax and accumulate near the equilibrium Fermi level (Figure 2c), and photocurrent arises from the extraction of these near-equilibrium carriers by either electric field or local temperature gradient.[12−15] However, the lack of photocurrent polarity reversal hints a different mechanism. Under pulse illumination, a high flux of photon excitation will create an excess amount of hot carriers. The relaxation of these hot carriers through scattering with optical phonon will quickly raise the optical phonon temperature to near hot carrier temperature, which becomes the bottleneck for thermal relaxation of hot carriers.[3,9] These processes lead to nonequilibrium hot carriers with elevated quasi-Fermi level (Figure 2d). As a result, hot carrier transport does not follow conventional mechanisms, and hot carrier photocurrent is proportional to its lifetime rather than the metal−graphene built-in electric field. Recent theoretical works predict that hot carrier lifetime will decrease with increasing intrinsic carrier density as Fermi energy moves away from the Dirac point.[22−24] Our observation of peak photocurrent at the Dirac point (Figure 2b) agrees with the prediction and provides evidence for the nonequilibrium hot carrier induced photocurrent in graphene. The exact mechanism for hot carrier extraction is unclear from this work. However, we speculate that the asymmetric electron and hole mobilities (μ_e/μ_h = 0.86 for the device shown in Figure 1b) can lead to hot electron and hole diffusion with different velocity. The resulting spatial charge distribution builds up the transient electric field, which drives the carriers to the contact. On-going works on devices with different metal contacts and different electron and hole mobilities are underway to elucidate the hot carrier extraction mechanism.

To gain further insight into the hot carrier dynamics, we studied the gate-dependent photocurrent at the metal/graphene junction under different pulse laser power. Figure 3a−c shows three representative photocurrent maps measured at 580 μW, 930 μW, and 3.49 mW pulse laser power, respectively. Significantly, photocurrent switches sign as the pulse laser power drops (Figure 3a), reminiscent of the case with CW excitation. More detailed power-dependent photocurrent curves

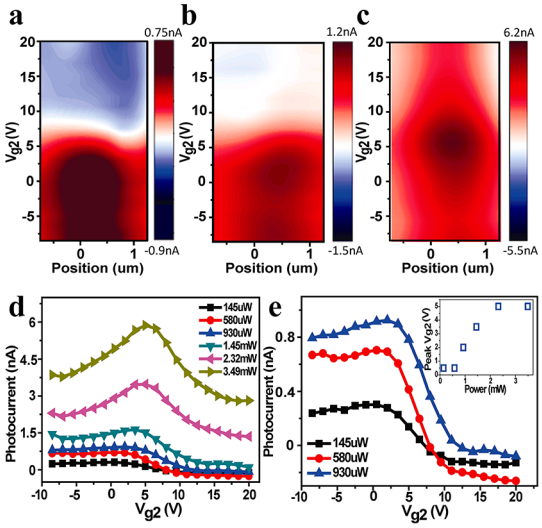

Figure 3. Power-dependent hot carrier photocurrent. (a−c) Gate-dependent photocurrent map under 580 μW (a), 930 μW (b), and 3.49 mW (c) pulse laser excitation. Position zero corresponds to the metal contact edge. (d) Gate-dependent photocurrent at the metal contact edge, excited by different pulse laser power. (e) Zoom-in view of the low photocurrent amplitude region. The inset shows the relation between photocurrent peak and pulse laser power.

obtained at the contact edge are shown in Figure 3d with the zoom-in view shown in Figure 3e. At a low power of 145 μW, photocurrent switches sign at $V_{g2} \sim$ 7.5 V, and positive photocurrent peaks around 0.5 V. These values are similar to the curve shown in Figure 2a, suggesting that built-in field and PTE dominate current generation. By increasing power to 580 μW, photocurrent amplitude increases in both positive and negative regions. However, at 930 μW, photocurrent becomes entirely positive and peaks at 2 V, indicating hot carrier extraction also contributes to photocurrent generation. With further increasing of the laser power, positive photocurrent peak gradually shifts to 5 V (Figure 3e, inset), at which point hot carriers dominate transport. The results indicate that hot carrier extraction is closely related to pulse laser illumination power.

We also studied the gate-dependent photocurrent generation within the graphene p−n junction formed by the split bottom gates. To identify the photocarrier transport mechanism, we compared the experimental data with simulations of field-driven carrier transport and PTE-originated transport in Figure 4. From the split gate responses of the device, we can calculate gate-dependent thermopower (Figure 4a) using the Mott formula:[16]

$$S = -\frac{\pi^2 K_B^2 T}{3e}\frac{1}{G}\frac{dG}{dE}_{E=E_f}$$

where S is thermopower and G is conductance. PTE-originated photocurrent is expected to be proportional to the thermal power difference, ΔS, across the p−n junction, as plotted in Figure 4b. If the photocarrier

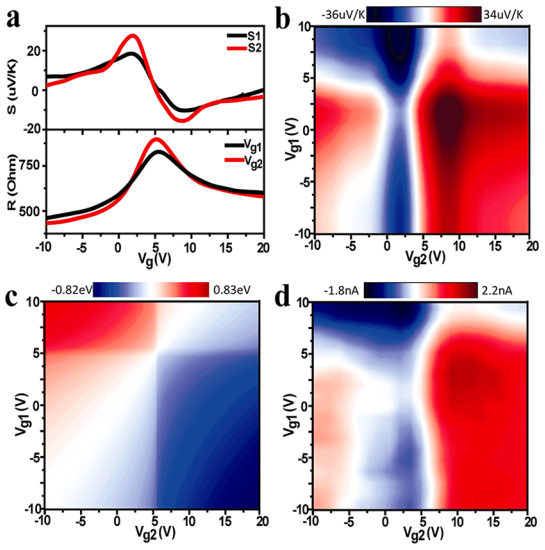

Figure 4. Gate-dependent photocurrent generation at the graphene p−n junction under CW excitation. (a) Split gate responses of the device (bottom panel) and the calculated gate-dependent thermopower (top panel). (b) Thermopower difference across the p−n junction under different split gate voltages. (c) Fermi energy difference across the p−n junction under different split gate voltages. (d) Measured gate-dependent photocurrent at the graphene p−n junction under 2 mW CW excitation.

transport is field-driven, then the photocurrent is expected to follow the Fermi energy difference across the p−n junction. We simulated the Fermi energy difference across the junction under different gate voltages using the split gate responses and plotted it in Figure 4c. The measured split gate voltage-dependent photocurrent under 2 mW CW excitation is plotted in Figure 4d. Clearly, the change of photocurrent polarity and peak shows excellent agreement with the simulation result of Figure 4b. PTE dominates photocurrent generation in the graphene p−n junction, consistent with recent theoretical prediction based on similar device configuration.[18]

Last, we investigated the disappearance of photocurrent at the graphene p−n junction under femtosecond pulse laser excitation, as previously shown in Figure 1d. To exclude the effect of gate biasing, we reversed the gate biasing condition by sweeping V_{g1} with V_{g2} fixed at 0 V. Again, there is no photocurrent generation from the p−n junction (Figure 5a). Complete dual gate sweeps with pulse laser excitation at the p−n junction show almost no photocurrent regardless of the dual gate voltages, as evident in Figure 5b (also see Supporting Information Figure S3). This result further corroborates the hot carrier nature of the photocurrent generation in graphene. Under pulse excitation, there is no hot carrier temperature gradient across the p−n junction due to the overheating phonon temperature,[18] and PTE photocurrent is significantly suppressed as a result.

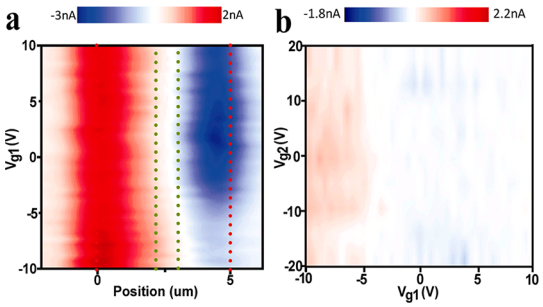

Figure 5. Gate-dependent photocurrent generation at the graphene p−n junction under pulse excitation. (a) V_{g1} gate-dependent photocurrent map of the device under 2 mW pulse excitation. Here V_{g2} is grounded. (b) Dual gate-dependent photocurrent map with pulse laser excitation at the graphene p−n junction.

CONCLUSIONS

In summary, we systematically study the photocurrent generation at the graphene−metal contact and graphene p−n junction. The striking difference between CW and pulse laser excitation reveals that graphene photoresponse is closely related to illumination intensity. Importantly, we demonstrate the possibility of extracting nonequilibrium hot carriers from graphene. This finding may pave a promising pathway to build graphene-based hot carrier optoelectronics. To improve the hot carrier extraction efficiency under low illumination intensity, hot carrier cooling rate could be further slowed by quantizing graphene energy states through fabricating graphene nanoribbons[26] or by opening a band gap in bilayer graphene.[27,28]

METHODS

Graphene was synthesized by chemical vapor deposition (CVD) method on copper[29] and then transferred to the prepatterned substrate. Single-layer nature of the graphene was identified by Raman spectroscopy. For the prepatterned substrate, Ti/Au (5/30 nm) was patterned on top of 300 nm thick silicon dioxide to serve as two split bottom gates. The pair of split gates is separated by 1 μm. Al_2O_3 (50 nm thick) was then deposited by atomic layer deposition (ALD) as the back gate dielectric. After graphene was transferred to this prepatterned substrate, the selected graphene channel areas were defined by oxygen plasma. Photolithography was then used to pattern source and drain contacts, and Ti/Au (5/50 nm) was deposited by electron beam evaporation. The source and drain contacts were separated by 5 μm. Finally, the entire graphene device was covered by 50 nm Al_2O_3, deposited by ALD, in order to keep the device stable under ambient conditions.

Conflict of Interest: The authors declare no competing financial interest.

Acknowledgment. We thank Profs. L. Jay Guo and P. C. Ku for sharing some of the equipment. This work was supported from the Donors of the American Chemical Society Petroleum Research Fund, the U-M/SJTU Collaborative Research Program in Renewable Energy Science and Technology, and National Science Foundation Scalable Nanomanufacturing Program

(DMR-1120187). Devices were fabricated in the Lurie Nanofabrication Facility at University of Michigan, a member of the National Nanotechnology Infrastructure Network funded by the National Science Foundation.

Supporting Information Available: Detailed device structure, electrical properties of the device, and scanning photocurrent spectroscopy. This material is available free of charge *via* the Internet at http://pubs.acs.org.

REFERENCES AND NOTES

1. Nair, R. R.; Blake, P.; Grigorenko, A. N.; Novoselov, K. S.; Booth, T. J.; Stauber, T.; Peres, N. M. R.; Geim, A. K. Fine Structure Constant Defines Visual Transparency of Graphene. *Science* **2008**, *320*, 1308–1308.
2. Mak, K. F.; Sfeir, M. Y.; Wu, Y.; Lui, C. H.; Misewich, J. A.; Heinz, T. F. Measurement of the Optical Conductivity of Graphene. *Phys. Rev. Lett.* **2008**, *101*, 196405.
3. Wang, H.; Strait, J. H.; George, P. A.; Shivaraman, S.; Shields, V. B.; Chandrashekhar, M.; Hwang, J.; Rana, F.; Spencer, M. G.; Ruiz-Vargas, C. S.; *et al.* Ultrafast Relaxation Dynamics of Hot Optical Phonons in Graphene. *Appl. Phys. Lett.* **2010**, *96*, 081917.
4. Bistritzer, R.; MacDonald, A. H. Electronic Cooling in Graphene. *Phys. Rev. Lett.* **2009**, *102*, 206410.
5. Strait, J. H.; Wang, H.; Shivaraman, S.; Shields, V.; Spencer, M.; Rana, F. Very Slow Cooling Dynamics of Photoexcited Carriers in Graphene Observed by Optical-Pump Terahertz-Probe Spectroscopy. *Nano Lett.* **2011**, *11*, 4902–4906.
6. Ruzicka, B. A.; Wang, S.; Werake, L. K.; Weintrub, B.; Loh, K. P.; Zhao, H. Hot Carrier Diffusion in Graphene. *Phys. Rev. B* **2010**, *82*, 195414.
7. Breusing, M.; Ropers, C.; Elsaesser, T. Ultrafast Carrier Dynamics in Graphite. *Phys. Rev. Lett.* **2009**, *102*, 086809.
8. Breusing, M.; Kuehn, S.; Winzer, T.; Malic, E.; Milde, F.; Severin, N.; Rabe, J. P.; Ropers, C.; Knorr, A.; Elsaesser, T. Ultrafast Nonequilibrium Carrier Dynamics in a Single Graphene Layer. *Phys. Rev. B* **2011**, *83*, 153410.
9. Dawlaty, J. M.; Shivaraman, S.; Chandrashekhar, M.; Rana, F.; Spencer, M. G. Measurement of Ultrafast Carrier Dynamics in Epitaxial Graphene. *Appl. Phys. Lett.* **2008**, *92*, 042116.
10. Lui, C. H.; Mak, K. F.; Shan, J.; Heinz, T. F. Ultrafast Photoluminescence from Graphene. *Phys. Rev. Lett.* **2010**, *105*, 127404.
11. Liu, W.-T.; Wu, S. W.; Schuck, P. J.; Salmeron, M.; Shen, Y. R.; Wang, F. Nonlinear Broadband Photoluminescence of Graphene Induced by Femtosecond Laser Irradiation. *Phys. Rev. B* **2010**, *82*, 081408.
12. Lee, E. J. H.; Balasubramanian, K.; Weitz, R. T.; Burghard, M.; Kern, K. Contact and Edge Effects in Graphene Devices. *Nat. Nanotechnol.* **2008**, *3*, 486–490.
13. Mueller, T.; Xia, F.; Freitag, M.; Tsang, J.; Avouris, P. Role of Contacts in Graphene Transistors: A Scanning Photocurrent Study. *Phys. Rev. B* **2009**, *79*, 245430.
14. Xia, F.; Mueller, T.; Golizadeh-Mojarad, R.; Freitag, M.; Lin, Y.-M.; Tsang, J.; Perebeinos, V.; Avouris, P. Photocurrent Imaging and Efficient Photon Detection in a Graphene Transistor. *Nano Lett.* **2009**, *9*, 1039–1044.
15. Park, J.; Ahn, Y. H.; Ruiz-Vargas, C. Imaging of Photocurrent Generation and Collection in Single-Layer Graphene. *Nano Lett.* **2009**, *9*, 1742–1746.
16. Xu, X.; Gabor, N. M.; Alden, J. S.; van der Zande, A. M.; McEuen, P. L. Photo-Thermoelectric Effect at a Graphene Interface Junction. *Nano Lett.* **2010**, *10*, 562–566.
17. Lemme, M. C.; Koppens, F. H. L.; Falk, A. L.; Rudner, M. S.; Park, H.; Levitov, L. S.; Marcus, C. M. Gate-Activated Photoresponse in a Graphene p–n Junction. *Nano Lett.* **2011**, *11*, 4134–4137.
18. Song, J. C. W.; Rudner, M. S.; Marcus, C. M.; Levitov, L. S. Hot Carrier Transport and Photocurrent Response in Graphene. *Nano Lett.* **2011**, *11*, 4688–4692.
19. Peters, E. C.; Lee, E. J. H.; Burghard, M.; Kern, K. Gate Dependent Photocurrents at a Graphene p–n Junction. *Appl. Phys. Lett.* **2010**, *97*, 193102.
20. Gabor, N. M.; Song, J. C. W.; Ma, Q.; Nair, N. L.; Taychatanapat, T.; Watanabe, K.; Taniguchi, T.; Levitov, L. S.; Jarillo-Herrero, P. Hot Carrier-Assisted Intrinsic Photoresponse in Graphene. *Science* **2011**, *334*, 648–652.
21. Sun, D.; Aivazian, G.; Jones, A. M.; Ross, J. S.; Yao, W.; Cobden, D.; Xu, X. Ultrafast Hot-Carrier-Dominated Photocurrent in Graphene. *Nat. Nanotechnol.* **2012**, *7*, 114–118.
22. Calandra, M.; Mauri, F. Electron–Phonon Coupling and Electron Self-Energy in Electron-Doped Graphene: Calculation of Angular-Resolved Photoemission Spectra. *Phys. Rev. B* **2007**, *76*, 205411.
23. Tse, W.-K.; Das Sarma, S. Phonon-Induced Many-Body Renormalization of the Electronic Properties of Graphene. *Phys. Rev. Lett.* **2007**, *99*, 236802.
24. Tse, W.-K.; Hwang, E. H.; Sarma, S. D. Ballistic Hot Electron Transport in Graphene. *Appl. Phys. Lett.* **2008**, *93*, 023128.
25. Winzer, T.; Knorr, A.; Malic, E. Carrier Multiplication in Graphene. *Nano Lett.* **2010**, *10*, 4839–4843.
26. Li, X.; Wang, X.; Zhang, L.; Lee, S.; Dai, H. Chemically Derived, Ultrasmooth Graphene Nanoribbon Semiconductors. *Science* **2008**, *319*, 1229–1232.
27. Zhang, Y.; Tang, T.-T.; Girit, C.; Hao, Z.; Martin, M. C.; Zettl, A.; Crommie, M. F.; Shen, Y. R.; Wang, F. Direct Observation of a Widely Tunable Bandgap in Bilayer Graphene. *Nature* **2009**, *459*, 820–823.
28. Lee, S.; Lee, K.; Zhong, Z. Wafer Scale Homogeneous Bilayer Graphene Films by Chemical Vapor Deposition. *Nano Lett.* **2010**, *10*, 4702–4707.
29. Li, X.; Cai, W.; An, J.; Kim, S.; Nah, J.; Yang, D.; Piner, R.; Velamakanni, A.; Jung, I.; Tutuc, E.; *et al.* Large-Area Synthesis of High-Quality and Uniform Graphene Films on Copper Foils. *Science* **2009**, *324*, 1312–1314.